Geomechanics and Engineering, *Vol. 15, No. 5 (2018) 1047-1059*
DOI: https://doi.org/10.12989/gae.2018.15.5.1047

Crack initiation and fragmentation processes in pre-cracked rock-like materials

Jooeun Lee and Jung-Wuk Hong*

Department of Civil and Environmental Engineering, Korea Advanced Institute of Science and Technology, Daejeon 34141, South Korea

(Received January 21, 2018, Revised January 28, 2018, Accepted January 29, 2018)

Abstract. This paper focuses on the cracking and fragmentation process in rock materials containing a pair of non-parallel flaws, which are through the specimen thickness, under vertical compression. Several numerical experiments are conducted with varying flaw arrangements that affect the initiation and tensile wing cracks, shear crack growth, and crack coalescing behaviors. To obtain realistic numerical results, a parallelized peridynamics formulation coupled with a finite element method, which is able to capture arbitrarily occurring cracks, is employed. From previous studies, crack initiation and propagation of tensile wing cracks, horsetail cracks, and anti-wing cracks are well understood along with the coalescence between two parallel flaws. In this study, the coalescence behaviors, their fragmentation sequences, and the role of an x-shaped shear band in rock material containing two non-parallel flaws are discussed in detail on the basis of simulation results strongly correlated with previous experimental results. Firstly, crack initiation and propagation of tensile wing cracks and shear cracks between non-parallel flaws are investigated in time-history and then sequential coalescing behavior is analyzed. Secondly, under the effect of varying inclination angles of two non-parallel flaws and overlapping ratios between a pair of non-parallel flaws, the cracking patterns including crack coalescence, fragmentation, and x-shaped shear band are investigated. These numerical results, which are in good agreement with reported physical test results, are expected to provide insightful information of the fracture mechanism of rock with non-parallel flaws.

Keywords: non-parallel flaws; progressive failure; crack coalescence; fragmentation; x-shaped shear band

1. Introduction

Since rock material has numerous non-persistent discontinuities including voids, holes, joints, and flaws, the discontinuities in rock material under stresses initiate propagation and coalescence with other growing flaws. This coalescence plays a critical role in undermining the strength of rock material, thereby causing deformation and subsequent failure. To investigate how newly growing cracks, such as tensile wing cracks or secondary shear cracks, initiate and propagate, numerous experiments on rock material containing a single flaw (a flaw is referred to as a pre-existing open crack) under compression have been carried out. For further study based on the general crack patterns of a single flaw, coalescence development sequences between a pair of flaws or among multiple flaws in rock materials have been analyzed through a number of physical experiments.

Types of fracturing patterns in specimens with a single flaw are observed under the effect of the flaw inclination angles. The initiation position of tensile wing cracks is shifted by changing the flaw angles (Wong 2008). The tensile wing crack initiates from the middle of the flaw surface when the flaw is aligned horizontally. However, with increasing angles, the initiation position is shifted to the flaw tips. Moreover, many researchers have listed crack types according to the different crack trajectories and the crack initiation mechanisms, such as tensile or shear modes, with varying flaw angles (Wong and Einstein 2009a). In addition, various patterns of shear cracks such as shear zones (Lajtai 1974), inclined/normal shear fractures, and anti-wing cracks (Wong *et al.* 2006) have been reported. After tensile wing cracks occur, shear cracks initiate at the flaw tips and develop an x-shaped shear band around each flaw tip at failure (Huang *et al.* 1990 and Chen *et al.* 1995). This x-shaped band results from the growth of horsetail cracks and anti-wing cracks that initiate at both tips of the flaw and subsequently propagate outwardly.

To investigate the effect of flaw arrangement on fracturing patterns, types of coalescing patterns in terms of the crack types (shear/tension crack, internal wing crack, and internal shear crack) and the coalescence crack surfaces (rough with crushed surface and clean with smooth surface) are categorized (Ko and Einstein 2006). In addition, various crack coalescence types between two parallel flaws are observed with respect to their overlapping ratio (Lee *et al.* 2017b). When the overlapping ratio is approximately zero, as illustrated in Fig. 1(a), an isolated crack segment occurs in the bridging region between two flaws and it is linked through two horsetail cracks emanating from the inner flaw tips (Shen *et al.* 1995). Moreover, the bridging angle between two flaws is approximately vertical, the relative sliding fracture surface induces tensile wing cracks to initiate at the flaw tips, and then the tensile wing cracks link the inner tips of two adjacent flaws (Cao *et al.* 2015). In an arrangement that is partially overlapped, an isolated, central fragmentation occurs in the bridging region between two inner tips of the flaws (Mughieda and Alzo'ubi 2004). As

*Corresponding author, Professor
E-mail: j.hong@kaist.ac.kr

http://www.techno-press.org/?journal=gae&subpage=7
ISSN: 2005-307X (Print), 2092-6219 (Online)

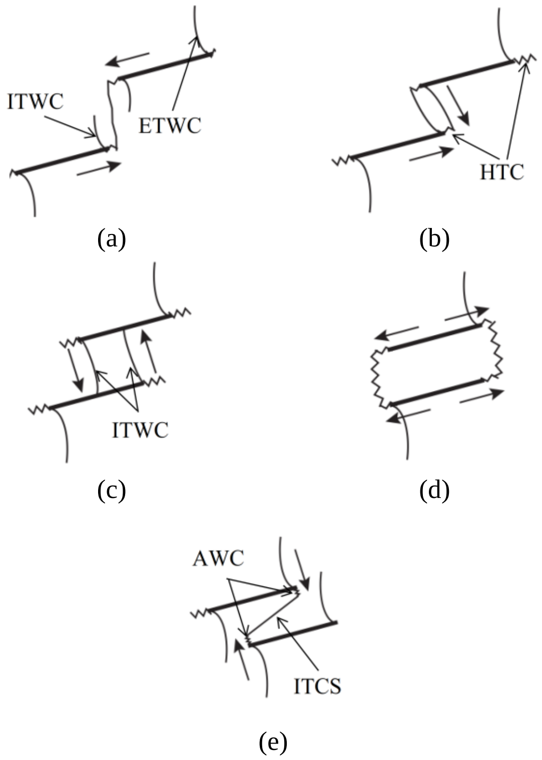

Fig. 1 Schematic illustration of coalescence types between two flaws with respect to their overlapping ratios, modified from Park and Bobet (2010) and Sagon and Bobet (2002) where internal tensile wing crack (ITWC), external tensile wing crack (ETWC), horsetail crack (HTC), isolated tensile crack segment (ITCS), and anti-wing crack (AWC) are described

the overlapping ratio of two flaws increases, as depicted in Figs. 1(b) and 1(c), each internal tensile wing crack initiates at the flaw surface normal to the tip of its opposite flaw (Lee *et al.* 2017b, Park and Bobet 2010, Sagong and Bobet 2002, Wong and Einstein 2009b, Cheng *et al.* 2015). This causes a fragmentation that is surrounded by these internal tensile wing cracks, as in Figs. 1(b) and 1(c), but the fragmentation ceases to deform in the bridging region even with further loading (Bobet and Einstein 1998, Cao *et al.* 2015). However, other cracks including horsetail cracks or anti-wing cracks initiate around flaw tips and then propagate in a sudden and unstable manner, leading to failure of the specimens, as illustrated in Fig.1d (Park and Bobet 2010). In a substantially overlapped arrangement, coalescence is formed through internal tensile wing cracks or a combination of horsetail cracks and an isolated tensile crack segment (Yang *et al.* 2012). As shown in Fig. 1(e), an isolated tensile crack occurs in a bridging region and then links in an unstable manner with shear cracks. In the specimens with more than two flaws, coalescence generally occurs between two relatively adjacent flaws and its patterns are consistent with those of flaw pairs (Sagong and Bobet 2002, Cao *et al.* 2015, Park and Bobet 2010, Lee *et al.* 2017c, Wong *et al.* 2001, Zhou *et al.* 2014, Park and Bobet 2009, Yang *et al.* 2012, Feng *et al.* 2009).

To complement these physical test results and enhance the understanding of the coalescence process between or among flaws, numerous numerical simulations have been carried out. The rock failure process analysis code (RFPA 2D) captured the initiation and growth of tensile wing cracks (Tang and Kou 1998), and reproduced the coalescence of tensile wing cracks caused by tensile mode, shear mode, or mixed mode. The method also showed the failure mechanism and four types of crack coalescence modes in rock material containing three flaws (Tang *et al.* 2001). The same method reproduced the crack evolution of a single flaw, three flaws, and multiple flaws (Wong *et al.* 2002). RFPA 2D reasonably captured the general patterns of tensile wing cracks initiating at the flaw tips and the coalescence among three and multiple flaws. The bonded particle model (BPM) reproduced that secondary cracks initiate under tensile stresses, and then under shear forces crack surfaces become rough and unclean (Manouchehrian and Marji 2012, Manouchehrian *et al.* 2014, Zhang and Wong 2013). The numerical method indicated that tensile wing cracks initiate at the flaw tips induced by tensile stresses and propagate upwards until secondary cracks occur under tensile stresses and then under shear forces soon. AUTODYN predicted the coalescence development in rock material with two flaws under the effect of flaw arrangements (Li and Wong 2014). With this method it was also observed that most of the cracks causing coalescence initiate at or around the flaw tips while the cracks inducing coalescence initiate at a point on the flaw surface in arrangements where two flaws are very close and substantially overlapped. The numerical manifold method (NMM) investigated the effects of pre-existing micro-crack length, inclination angle, and separation distance on the dynamic mechanical properties of rock (Wu and Wong 2014). The particle flow code (PFC) indicated the crack growth process along with parallel bond force field in rock material and also identified that crack coalescence results from the bond force affected by the crack initiation (Tian and Yang 2017). The method reproduced coalescence development sequences between two parallel flaws whose ligament angles were varied (Sarfarazi and Haeri 2016, Haeri *et al.* 2017). A numerical simulation using the general particle dynamics (GPD) captured coalescence development sequences in rock material with four flaws (Zhou *et al.* 2015). The method showed that the coalescence formed by tensile wing cracks is a relatively smooth path and that pure shear coalescence is created by coplanar or quasi-coplanar cracks (referred to as horsetail cracks in this paper). It also reproduced that the shear band or zone is caused by oblique secondary cracks (as anti-wing cracks).

These physical and numerical experiments have been conducted to study crack patterns or crack coalescence of a single, two flaws, or multiple flaws in rock materials under compression. The effect of flaw inclination angles and the effect of the flaw arrangements and their overlapping ratios have been investigated in detail. However, these experiments are confined to the arrangement of parallel flaws. Investigation of fracturing patterns in more complicated flaw geometries (Li and Wong 2014) such as coalescence among non-parallel open flaws would thus be useful. In this light, the present paper focuses on crack growth and coalescence between two non-parallel open flaws with the help of peridynamics. To understand

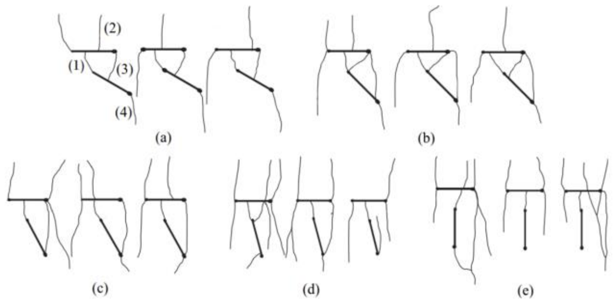

Fig. 2 Sketches of the physically observed coalescing patterns between two non-parallel flaws of which the inclination angles of the lower flaw increase with an interval of 15° from 30° to 90°, modified from Lee and Jeon (2011). (a) 30°, (b) 45°, (c) 60°, (d) 75°, and (e) 90°. The numbers indicate types of newly creating cracks: An internal tensile wing crack (1) and an external tensile wing crack (2) both initiate from the upper flaw, while an internal tensile wing crack (3) and an external tensile wing crack (4) initiate from the lower flaw.

deformation and progressive failure, including crack coalescence development sequences and shear crack behaviors between two non-parallel flaws, the effect of both the overlapping ratio of two flaws and the inclination angles of two non-parallel flaws on cracking development process is discussed in detail. The numerical results are expected to enhance the understanding of the crack evolution and coalescing process in rock material with two non-parallel flaws.

2. Coalescence processes between two non-parallel flaws

2.1 Brief description of experimental results

General coalescence patterns between two non-parallel flaws in rock material under a vertical load are described in Fig. 2, where internal tensile wing cracks play a central role in the coalescence development sequences. They performed physical experiments on rock material with two non-parallel flaws whose geometry varied as the inclination angle of the lower flaw (α) increased with an interval of 15° from 30° to 90°, as described in Fig. 2. As shown in Fig. 2(a), the external tensile wing crack (2) initiates from the middle of the upper flaw whose inclination angle is 0°, and it then propagates parallel to the direction of vertical loading. Generally, the external tensile wing crack emanating from the upper surface at or near the middle of the upper flaw proceeds vertically as in Figs. 2(a)-2(e). However, unlike the propagation path of the tensile wing crack initiating from the lower surface of the horizontal flaw, the internal tensile wing crack (1) initiating from the upper flaw propagates vertically but curves towards the left tip of the lower flaw under the interaction effect between two flaws. In addition, the internal tensile wing crack (3) occurs at the middle upper surface of or at the left tip of the lower flaw and propagates towards the right tip of the upper flaw, thereby leading to coalescence. Interestingly, each of the two internal tensile wing cracks coalesces with the other flaw, forming a fragmentation that is not damaged even with further loading, as shown in Figs. 2(a)-2(d).

The test results present general coalescence patterns with varying inclination angles of the lower flaw. However, the results do not take into account the coalescence development sequences between two non-parallel flaws or the initiation and propagation of shear cracks and wing cracks under their corresponding interaction effect. This study, through the help of parallelized peridynamics (Lee *et al.* 2017a), discusses the coalescing processes of cracks and the initiation position of tensile wing cracks and shear cracks, including horsetail cracks and anti-wing cracks, under the interaction effect of other growing cracks.

2.2 Overview of peridynamic formulation

In this study, the parallelized peridynamic code coupled with the finite element method, which shows a good ability to realistically represent fracturing behaviors in rock material in Refs. (Lee *et al.* 2017a, b, 2016a, Lee and Hong 2016b), is used. The numerical method is described in detail by Lee et al (2017a) and Liu and Hong (2012a, b, c), and an overview of its essential features is briefly introduced as follow.

For reformulation of the classical continuum model where partial differential equations are used, the peridynamic equation at the reference configuration of position **x** at a time t is expressed as (Silling 2000, Silling and Askari 2005)

$$\int_{H_x} \mathbf{f}(\boldsymbol{\eta},\boldsymbol{\xi})\,dV_{\mathbf{x}'} = \rho\,\ddot{\mathbf{u}}(\mathbf{x},t) - \mathbf{b}(\mathbf{x},t). \tag{1}$$

In Eq.(1), $\int \mathbf{f}(\boldsymbol{\eta},\boldsymbol{\xi})$ is a pairwise force vector in terms of the relative displacement vector ($\boldsymbol{\eta} = \mathbf{u}(\mathbf{x},t) - \mathbf{u}(\mathbf{x},t)$) between two points and the relative position vector ($\boldsymbol{\xi} = \mathbf{x}' - \mathbf{x}$), along with an infinitesimal volume interacting with a particle at $\mathbf{x}'$ expressed as $dV_{\mathbf{x}'}$ and a prescribed body force vector expressed as $\mathbf{b}$. The spherical subregion (H_x) where neighboring particles interact with a particle positioned at $\mathbf{x}$ is controlled by a variable called horizon (δ), which expresses the nonlocal interaction size. Therefore, when the relative position vector (ξ) is within the horizon, the pairwise force vector exists. In addition, the relative bond stretch between two particles in Eq.(2) determines whether the pairwise force exerts within the horizon

$$s(\boldsymbol{\eta},\boldsymbol{\xi}) = \frac{\|\boldsymbol{\eta}+\boldsymbol{\xi}\| - \|\boldsymbol{\xi}\|}{\|\boldsymbol{\xi}\|}. \tag{2}$$

If the bond stretch between two particles (s) is shorter than the critical bond stretch (s_0) in Eq. (3), the stretch is proportional to the pairwise bond force. The horizon (δ) represents the size of the nonlocal interaction. The critical bond stretch is obtained from the energy release rate (G_0), which is the energy per unit fracture area required to break all the bonds connecting two hemispheres of a body (Silling and Askari 2005) with the micro-modulus function (c).

$$s_0 = \sqrt{\frac{10G_0}{\pi c \delta^5}}, \tag{3}$$

When the relative stretch is larger than the critical stretch, the bond connecting two particles is broken, leading to a softening material response and subsequently a sequential failure of interacting bonds; it then occurs as a surface crack induced through the coalescence of broken bonds. From the start of crack nucleation, the number of negligible pairwise forces among particles increases with further loading, thereby promoting crack growth.

$$\rho \ddot{\mathbf{u}}_i^t = \sum_{j=1}^{j=N_{H_i}} \mathbf{f}(\boldsymbol{\eta}^t, \xi) V_j + \mathbf{b}_i^t, \tag{4}$$

where $\ddot{\mathbf{u}}_i^t$ denotes the acceleration of node i at time t, $\mathbf{f}(\boldsymbol{\eta}^t, \xi)$ the pairwise force, N_{H_i} the total number of nodes within the horizon (δ) of node i, and $\mathbf{b}_i^t$ the body force at time t. For the temporal integration to update positions, velocities, and accelerations, the velocity-Verlet scheme (Ercolessi 1997) is used.

$$\mathbf{F}^{int} = \sum_e \mathbf{F}^{int(e)} = \sum_e \mathbf{K}^{(e)} \mathbf{U}^{(e)}. \tag{5}$$

For the efficiency of numerical simulation, a CT-coupling scheme was suggested by Liu and Hong (2012c), where the internal forces ($\mathbf{F}^{int}$) exerted on finite element nodes are obtained from Eq. (5) in which $\mathbf{K}^{(e)}$ is the element stiffness matrix and $\mathbf{U}^{(e)}$ is the nodal displacement vector. The motion equation of a finite element node is expressed as

$$\mathbf{M}_i \ddot{\mathbf{U}}_i = \mathbf{F}_i^{ext} - \mathbf{F}_i^{int}, \tag{6}$$

where $\mathbf{M}_i$ is the lumped mass for the node i, $\ddot{\mathbf{U}}_i$ is the acceleration vector field, and $\mathbf{F}_i^{ext}$ and $\mathbf{F}_i^{int}$ are the external and internal force vectors of node I, respectively. To couple the finite element (FE) subregion and the peridynamic (PD) subregion, an overlapping interface was introduced, as demonstrated in Fig. 3.

For the calculation of the coupling force that is subsequently distributed onto the FE nodes, the interacting forces between the PD nodes that are embedded in this overlapped region and the PD nodes in the PD subregion within the horizon size are expressed as the coupling force. To distribute the coupling force onto the FE nodes within the overlapped region between two distinct FE and PD subregions, as illustrated in Fig. 3, the coupling force is obtained from

$$\mathbf{f}_i^{cp} = \phi_i(\xi_c, \eta_c)\mathbf{f}^{cp}, \quad i = 1, 2, 3, 4, \tag{7}$$

where $\mathbf{f}_i^{cp}$ is the coupling force, ϕ_i is the shape function, and (ξ_c, η_c) is the natural coordinates of the projection of an overlapped nodes, which are all on the overlapped region. Hence, the internal force associated with node i of the overlapped region is expressed as

$$\hat{\mathbf{F}}_i^{int} = \mathbf{F}_i^{int} + \mathbf{f}_i^{cp} = \left[\sum_e \mathbf{K}^{(e)} \mathbf{U}^{(e)}\right]_i + \mathbf{f}_i^{cp}. \tag{8}$$

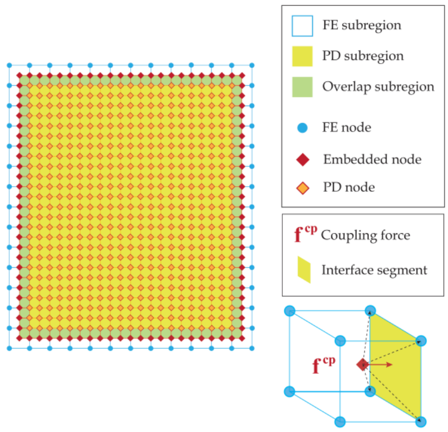

Fig. 3 Sketch of CT-coupling scheme.

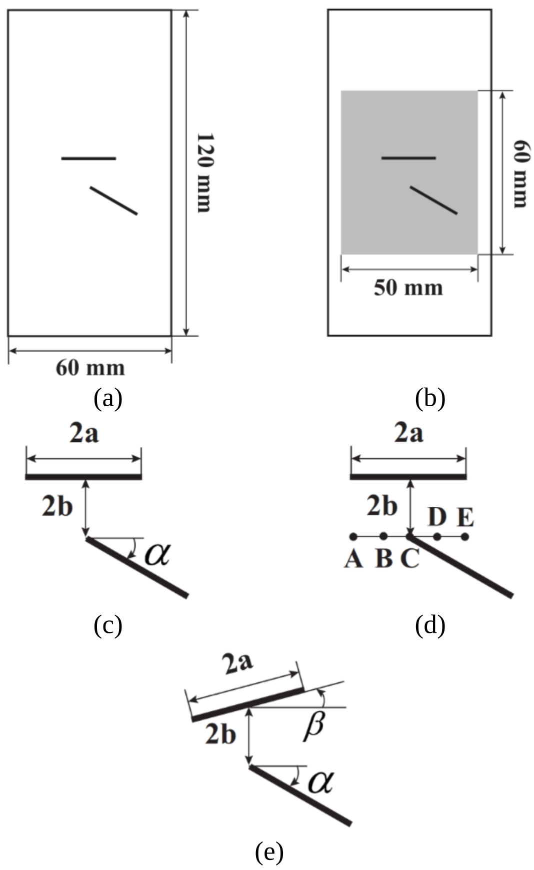

Fig. 4 Schematic illustrations of a specimen containing two non-parallel flaws. (a) flaw geometry in rock material and (b) a PD region where fracturing patterns are to be observed is modeled in all simulations. (c) to (e) are magnified snapshots of two non-parallel flaws in a specimen, (c) varying inclination angles (α) of the lower flaw, (d) varying positions (A, B, C, D, E) of the left tip of the lower flaw and (e) varying inclination angles of both the upper flaw (β)and the lower flaw (α)

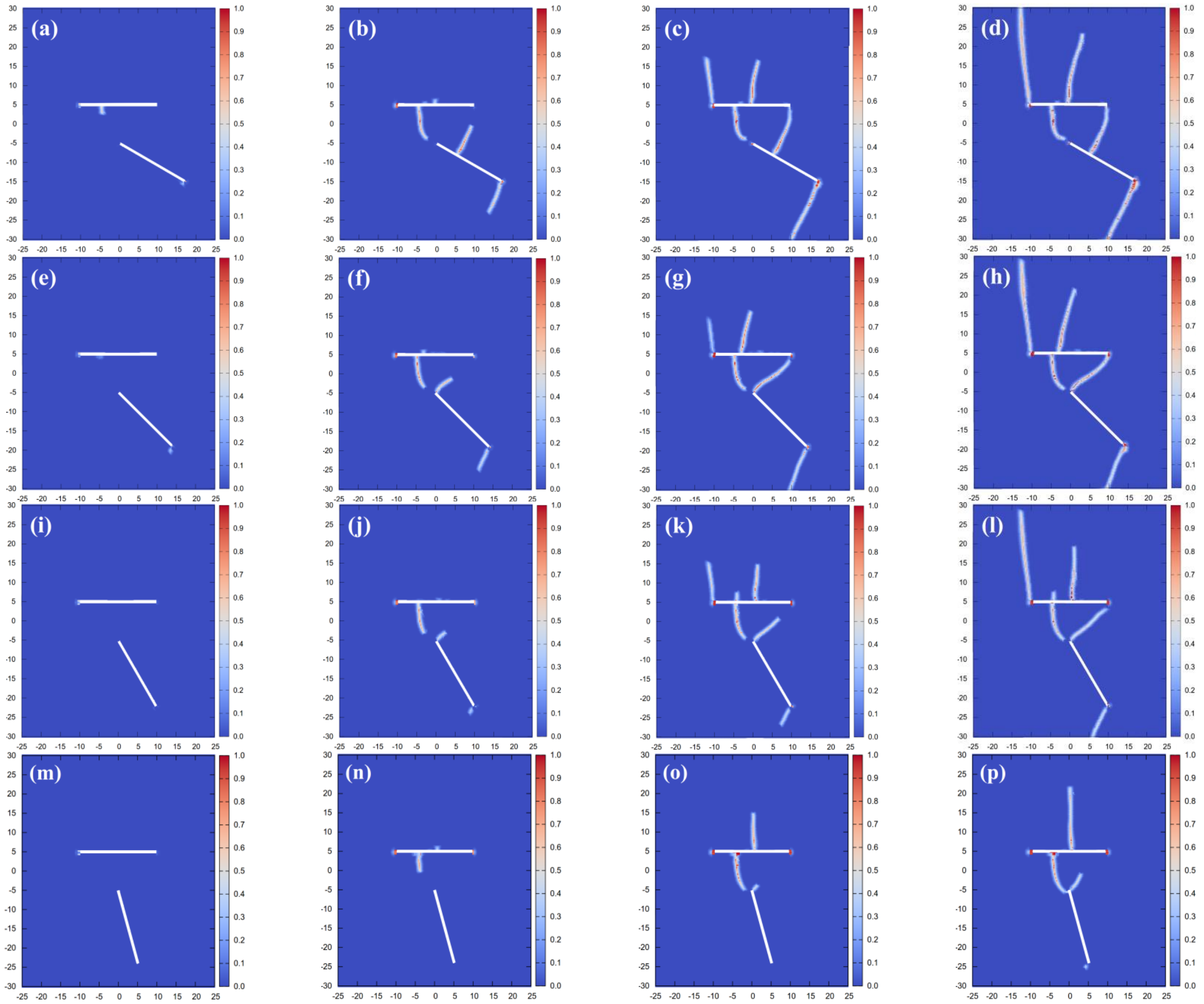

Fig. 5 Coalescence development sequences between two non-parallel flaws with varying inclination angles of the lower flaw (α) ranging from 30° to 75°. From (a) to (d) α=30°, (e) to (h) α=45°, (i) to (m) α=60° and (n) to (q) α=75°. The first column (a, e, i, and m) is captured at 32MPa, the second column (b, f, j, and n) at 40 MPa, the third column (c, g, k, and o) at 48 MPa, and the fourth column (d, h, l and p) at 56 MPa. Each damage map for all specimens is captured at the middle of the specimen along the vertical direction

2.3 Numerical procedure

Parallelized peridynamic code coupled with a finite element method has been used to analyze crack growth and coalescence in rock material (Lee *et al.* 2017b, Lee *et al.* 2017a, Lee and Hong 2016a, Ha *et al.* 2015). In this model, neighboring nodes within the horizon of a central node are connected through a bond. If the relative derivative of the bond distance between two nodes is beyond the critical bond stretch, the bond between nodes is broken and no longer sustains a load. This leads to softening material responses of rock, subsequently causing the bonds between a node and its neighboring nodes to be sequentially broken. As a crack initiates and then propagates, the number of broken bonds between a node and a neighboring node within the horizon also increases, which leads to crack growth (Ha *et al.* 2015). Peridynamics shows a good capacity to capture arbitrarily occurring cracks without prior knowledge or help of other mathematical methods.

This research focuses on crack growth and coalescence between two non-parallel flaws with the help of parallelized peridynamics code coupled with a finite element while comparing physical test results.

The numerical models employed in this paper are pre-cracked rectangular prismatic specimens whose dimensions are 120 mm in height, 60 mm in width, and 30 mm in depth and which contain two non-parallel open-through flaws that are 20 mm in length and 1 mm in width, as illustrated in Fig. 4. The geometry of the numerical specimen conducted by peridynamics corresponds with the geometry of the physical specimens. The variable 2a denotes the length of a flaw (20 mm) and 2b is the bridging distance between two flaws and is half the flaw length, or 10 mm. The specimen material which has a Young's modulus of 49.0 GPa, a Poisson's ratio of 0.25, an energy release rate of 71 J/m^2, and density of 2700 Kg/m^3 (Wong 2008, Lee *et al.* 2017b, Ha *et al.* 2015). With the CT-coupling scheme, as illustrated in Fig. 3, the specimen is partitioned into one peridynamic (PD) region and one finite element (FE) region surrounding the PD region, which is set to 60 mm in height, 60 mm in width, and 30 mm in depth, as shown in Fig. 4(c). Through simulations, the numerical results are based on uniform grids with 0.25 mm, which produces about 6,301,897 nodes. The convergence value, or the ratio of the horizon to the grid spacing, (Ha and Bobaru 2011) is 4, the micro-modulus c is 2.17×10^{23}N/m^6, and the critical bond stretch s_0 is 1.10×10^{-3}. To lessen the computational burden, parallelized peridynamic code coupled with a finite element method (Lee *et al.* 2017a) is executed, which makes the computation time until failure 30 times faster than when the sequential code is performed, on a multi-core system based on a Dual Intel ® Xeron(R) CPU E5-2687 v2 @ 3.40 GHz with 64 GB RAM with 32 threads. The load gradually increases until failure at a loading rate that is within the range of low loading rates recommended by Ref. (Li and Wong 2012) and numerically confirmed by Refs. (Ha *et al.* 2015, Lee *et al.* 2017b, Zhang and Wong 2013). A uniform time-step is set as t=0.1 μs while the damage data are produced every t=2 μs.

2.4 Crack coalescence development sequence and subsequent fragmentation

To compare and complement the physical test results, numerical experiments on nine specimens with a non-parallel flaw geometry, where the inclination angle of the lower flaw (α) increases, as presented in Fig. 4(c), with an interval of 15° from -30° to 90°, are carried out. Coalescence development sequences in four specimens are observed in Fig. 5. At the bar scale in Figs. 5-12, the value of 1.0 denotes that all neighbors exceed the critical bond stretch s_0, which means all bonds are broken. However, if some neighbors are below the critical bond stretch, the value is between 0.0 and 1.0. At the initial stages the internal tensile wing crack (ITWC) initiates from the lower surface near the middle of the upper surface earlier than other cracks. As the inclination angle of the lower flaw increases, the internal tensile wing crack (ITWC) of the upper flaw occurs later.

As for coalescence, the internal tensile wing crack (ITWC) of the upper flaw initiates and propagates towards the left tip of the lower flaw. While the ITWC grows, the external tensile wing crack (ETWC) initiating from the upper surface at the middle of the upper flaw initiates upwards. As the load increases, the ITWC bridges the lower surface of its upper flaw and the left tip of the lower flaw, showing the first coalescence in specimens. For the second coalescence, the ITWC initiates near the upper surface of the lower flaw in Fig. 5(b) or at the left tip of the lower flaw in Figs. 5(f), 5(j), and 5(o). The ITWC propagates, to some extent, perpendicular to the surface of the lower flaw (Figs. 5(b), 5(f), 5(k), and 5(o)) and then approaches the right tip of the upper flaw (Figs. 5(d), 5(h), and 5(l)), making the second coalescence. Surrounded by two coalescences (one is made by the ITWC of the upper flaw and the other is formed by the ITWC of the lower flaw), a fragmentation is formed in Figs. 5(d), 5(h), and 5(l), which was also observed in the results of physical experiments shown in Fig. 2. The fragmentation becomes slightly damaged even with further loading, while increasing loading induces initiation and propagation of other shear cracks. As the inclination angle of the lower angle increases, the initiation

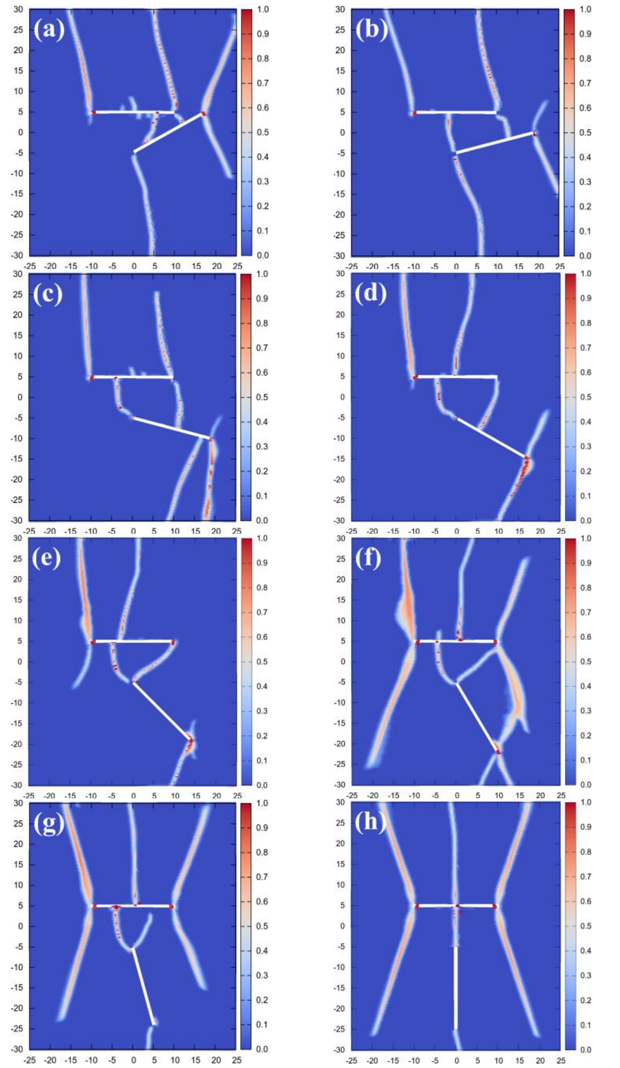

Fig. 6 Coalescence and an x-shaped shear band shear that shear cracks induce. (a) the inclination angle of the lower flaw is α=-30° and is captured at 67.2 MPa, (b) α=-15° and 56 MPa, (c) α=15° and 56 MPa, (d) α=30° and 67.2 MPa, (e) α=45° and 75.2 MPa, (f) α=60° and 86.4 MPa, (g) α=75° and 84.8 MPa and (h) α=90° and 84.8 MPa

position of the internal tensile wing crack shifts from the middle of the lower flaw to the left tip of the lower flaw, leading to a smaller area of fragmentation in Figs. 5(d), 5(h), 5(l), and 5(p) as well as in Figs. 2(a), 2(b), and 2(d). The inclination angle of the lower flaw influences the temporal sequence of initiation and propagation of tensile wing cracks and the fragmentation shape surrounded by two ITWCs.

2.5 Initiation and propagation of shear cracks and an x-shaped shear band

While each ITWC coalesces with the tips of the other flaw and forms a fragmentation, some shear cracks initiate at the outer tips of two non-parallel flaws, the left tip of the upper flaw and the right of the lower flaw. The initiation of a shear crack retards the growth of the tensile wing crack at the same position where the shear crack and tensile wing crack initiate. Therefore, as the load increases, the fragmentation made through two internal tensile wing cracks undergoes no further damage. At the left tip of a single flaw, a horsetail crack (HTC) initiates and propagates upwards while at the same tip an anti-wing crack (AWC) initiates and propagates downwards (Bobet 2000 and Wong 2008). In addition, at the right of a single flaw, a horsetail crack (HTC) initiates and propagates downwards while an anti-wing crack (AWC) proceeds upwards in the opposite direction of tensile wing crack propagation. As shown in Fig. 6(a), an ITWC initiates from the lower surface near the middle of the upper flaw and approaches the upper surface near the left tip of the lower flaw. Another ITWC initiates from the upper surface near the right tip of the lower flaw and reaches the right tip of the upper flaw. These coalescences form a fragmentation in the bridging region between two non-parallel flaws through tensile wing cracks (TWC), which is clearly shown in Figs. 6(a)-6(g). While the fragmentation occurs, ETWCs initiating both from the right tip of the upper flaw and from the left tip of the lower flaw reach the boundaries of a specimen. During the propagation of ETWCs, each HTC initiates from the left tip of the upper flaw and from the right tip of the lower flaw (in Fig. 6(a)) and then propagates in an unstable and fast manner, thereby reaching the boundary of a specimen.

Furthermore, each AWC initiates from the same position where its corresponding HTC occurs and propagates relatively faster than other cracks. Through the propagation of HTCs and AWCs initiating from the left tip of the upper flaw and from the right tip of the lower flaw, an x-shaped shear band is formed, as shown in Fig. 6(h). With further loading, this x-shaped shear band is numerically observed in all specimens as well as in physical tests.

2.6 Comparison of fracturing patterns

In rock material containing two non-parallel flaws under uniaxial compression, an external tensile wing crack generally initiates at or near the middle of the upper surface of the upper flaw because the upper flaw is aligned horizontally. In physical tests in Figs. 7(a)-7(c), the ETWC emanates from around the middle of the upper flaw surface and then propagates vertically towards the top edge of a specimen, which has been observed in many tests (Ha *et al.* 2015 and Wong 2008). Before the ETWC grows, internal tensile wing cracks initiate around the middle of the lower surface of the upper flaw.

The ITWC initiating from the upper flaw approaches the left tip of the lower flaw while the ITWC initiating from the lower flaw reaches the right tip of the upper flaw, then showing a fragmentation circumscribed by two ITWCs. This fragmentation is physically observed in Figs. 7(a), 7(b), and 7(d) and is also numerically confirmed in Figs. 7(e) to 7(h). The fragmentation area becomes smaller as the inclination angle of the lower flaw increases, which is due to the shift of the initiation position at which ITWC initiates from the upper surface of the lower flaw. In Figs. 7(a) and 7(e), the ITWC initiates at the middle of the upper surface of the lower flaw whose inclination angle is α =30°, but with the other inclination angles the initiation position is shifted to the left tip of the lower flaw. Another ETWC initiates from the right tip of the lower flaw and reaches the bottom of the specimen. As for shear cracks, the shear

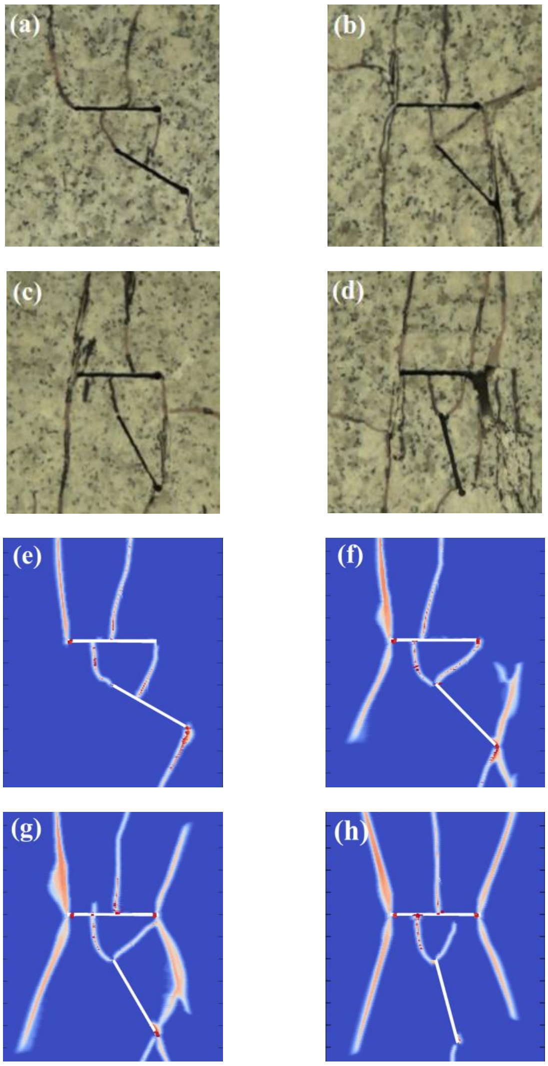

Fig. 7 Crack propagation and coalescence between two non-parallel flaws in rock material. The upper row (a) to (d) is from Lee and Jeon (2011). (a) and (e) are fracturing patterns with a lower flaw of α=30°, (b) and (f) are fracturing patterns with the lower flaw of α=45°, (c) and (g) are fracturing patterns with a lower flaw of α=60°, and (d) and (h) are fracturing patterns with a lower flaw of α=75°. (e) captured at 64 MPa, (f) at 80 MPa, (g) at 86.4 MPa, and (h) at 86.4 MPa

cracks in general initiate at the outer flaw tips, including the left tip of the upper flaw and the right tip of the lower flaw. From the left tip of the upper flaw, two types of shear cracks initiate; a HTC propagates upwards earlier than an AWC propagates downwards. Similarly, at the right tip of the lower flaw, a HTC propagates downwards as the ETWC does, while an AWC with further loading propagates upwards in the opposite direction of the ETWC at the right tip of the lower flaw. As the load increases, the shear cracks emanating from the left tip of the upper flaw reach the top and bottom of the specimen, showing half of the x-shaped band. At the right tip of the lower flaw, the HTC simply reaches the bottom of the specimen, but the AWC in most cases propagates in a relatively fast and unstable manner upwards and its path then becomes broader, which is

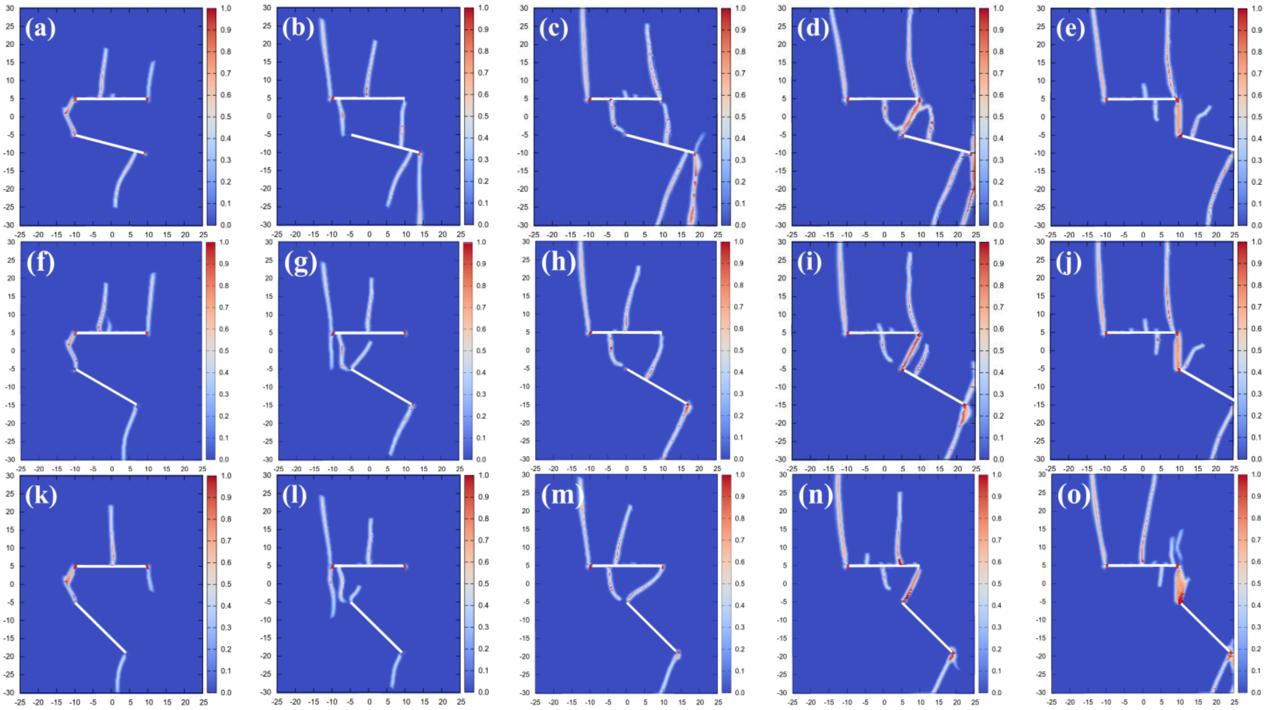

Fig. 8 Coalescing pattern with varying overlapping ratios between two non-parallel flaws, which is all captured at 56 MPa. The first row (a to e) is for the inclination angle of the lower flaw α=15°, the second row (f to j) is for α=30°, and the third row (k to o) is for α=45°. As for overlapping ratios, the first column is for the raio of 1.00; the second column is for 0.75; the third column is for 0.50; the fourth column is for 0.25; and the fifth column is for 0.00

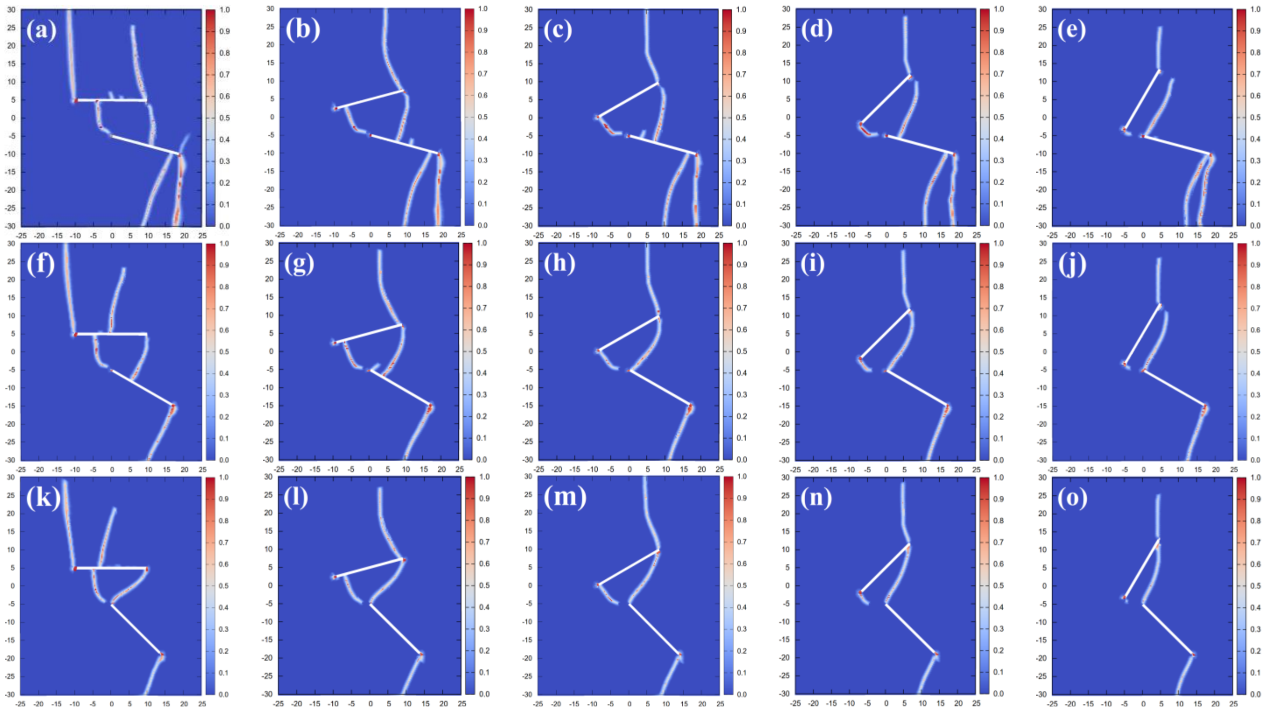

Fig. 9 Coalescing pattern with varying inclination angles of the upper flaw with an interval of 15° from β=0° to β=60°, which is captured in all specimens at 56 MPa. As for the inclination angle of the upper flaw, the first column is for β=0°, the second is for β=15°, the third is for β=30°, the fourth is for β=45°, the fifth is for β=60°. Also, for the inclination angle of the lower flaw, the first row (a to e) is for α=15°, the second row (f to j) is for α=30°, and the third row (k to o) is for α =45°

subsequently under the interaction effect. Fig. 7(f) shows that one branch emanates from the main AWC and propagates towards the right tip of the upper flaw, thereby leading to coalescence through a shear crack. Similarly, the coalescence caused through an AWC forms the second fragmentation, which is then deformed with further loading due to the swelling of the AWC in Fig. 7(g). These fracturing patterns were captured in physical tests, as shown in Figs. 7(b), 7(c), and 7(d). As observed in Fig. 7, the numerical simulations, through the help of the parallelized peridynamics coupled with a finite element method, have a good capability of capturing coalescence development sequences and show high fidelity to the physical tests. This numerical method is useful to predict fracturing patterns in complex flaw geometries such as a pair of non-parallel flaws.

3. Crack coalescence and fragmentation

Although there has been strong interest in coalescence between or among non-parallel flaws in rock material, there has been relatively little study of other critical factors, such as the overlapping ratio between two adjacent non-parallel flaws or non-parallel flaws whose inclination angles are varied. In response, under the effect of various effects, the coalescence created through tensile wing cracks is discussed in detail in this paper. In addition, the role shear cracks play in coalescing processes between two non-parallel flaws is investigated.

3.1 Overlapping ratios between non-parallel flaws

The effect of overlapping ratio on coalescing patterns between or among parallel flaws has been extensively studied, but fracturing patterns in non-parallel flaws under the overlapping effect have not been thoroughly parsed through physical tests. To describe the influence of the overlapping ratios between adjacent flaws on coalescence development, five different positions (A, B, C, D, and E) where the left tip of the lower flaw is located are set, as illustrated in Fig. 4(d). By changing these positions, the overlapping ratio with respect to the length of the upper horizontal flaw decreases from 1.00 at A to 0.00 at E with an interval 0.25; for example, the value 1.00 means that the lower flaw is fully overlapped with respect to the upper flaw length. As for the case where the lower flaw is fully overlapped, as in Figs. 8(a), 8(f), and 8(k), an ITWC initiates at the left tip of the lower flaw earlier than other cracks. An ETWC then initiates not at but near the right tip of the lower flaw due to the low inclination angle of the flaw, 15°. The ITWC propagates in the direction above 50° with respect to a horizontal line and subsequently coalesces with a shear crack that suddenly initiates from the left tip of the upper flaw. Because the coalescence is created through the linkage of an ITWC and a shear crack, the coalescence becomes more unstable and deformed with further loading, thereby severely damaging the specimen.

The ETWC emanating from the lower flaw propagates towards the bottom of the specimen as does the tensile wing crack (TWC) of a single flaw without any interacting effect between two flaws (Bobet 2000, Wong 2008, Ha *et al.* 2015). Similarly, another ETWC initiates around the middle of the upper surface of the upper flaw and then propagates upwards. As the load increases, shear cracks initiate from both tips of each flaw, and some of them coalesce with the right tip of the upper flaw and the right tip of the lower flaw, showing one fragmentation surrounded by the left and right coalescences. This is discussed in detail later. For cracking patterns in the first row for 15° with varying overlapping ratios, the initiation position of the internal tensile wing crack emanating from the upper flaw is shifted from the left tip of the upper flaw in Fig. 8(b) to around the middle of the lower surface of the upper flaw in Fig. 8(e), which is also observed in the second and third rows. Without the effect of the inclination angle of the flaw, the initiation position is shifted solely under the effect of overlapping ratios between two flaws. Another ITWC initiates at the left tip of the lower flaw in the case of a fully overlapped flaw geometry, including Figs. 8(a), 8(f), and 8(k), in part due to the adjacent distance between two flaws. However, with the overlapping ratio decreasing from 0.75 to 0.25, as described in Fig. 4(d), the ITWC initiates from the upper surface of the lower flaw, and it propagates nearly perpendicular to the lower flaw surface. For the initiation position of the ITWC of the lower flaw, as the ratio decreases from 0.75 to 0.25, or from Fig. 8(b)-8(d), the initiation position is shifted from near the right tip of the lower flaw to near the left tip of the flaw. In Fig. 8(b) and Fig. 8(c), the ITWC reaches the right tip of the upper flaw, leading to coalescence. However, in Fig. 8(d) and Fig. 8(e), an isolated tensile crack segment (ITCS) suddenly occurs in the bridging area between two flaws, then linking the two flaws, while the ITWC initiating from the lower flaw joins the existing coalescence in Fig. 8(d) or propagates upwards without any interaction in Fig. 8(e). As the overlapping ratio decreases, the fragmentation area circumscribed by two coalescences also becomes smaller. In the case where the overlapping ratio is 1.00, or corresponding with the first column in Fig. 8, the fragmentation is made through the linkage of two coalescences induced by shear cracks, although the ITWC initiating from the left tip of the lower flaw approaches the left tip of its opposite flaw. For the overlapping ratios of 0.75 and 0.50, the fragmentation is created by two coalescences, both of which are formed by corresponding internal tensile wing cracks. For the ratio of 0.25 or the fourth column, an ITCS occurs in the bridging region between two flaws, leading to coalescence, along with other coalescences by tensile wing cracks. Furthermore, in the case of the ratio of 0.00, or corresponding with the fifth column in Fig. 8, fragmentation is not observed, but the coalescence by the sudden growth of an isolated crack segment becomes wider with further loading. Therefore, it is observed that the overlapping ratio between two non-parallel flaws influences crack modes for fragmentation and it subsequently changes the overall fracturing patterns in specimens.

3.2 Inclination angles of the upper and lower flaws

To investigate cracking behaviors in more complex flaw geometries, the upper flaw is rotated at the center of the flaw anticlockwise with an interval of 15° from β=0° to β=60°, along with changing inclination angles of the lower flaw (α=15°, α=30°, and α=45° clockwise). As observed in the first row in Fig. 9, interestingly the initiation position at which an ITWC occurs is shifted from the middle of the upper surface of the lower flaw in Fig. 9(a) to near the left tip of the flaw in Fig. 9(d), and then to the left tip of the flaw in Fig. 9(e). However, the initiation position of the lower flaw whose inclination angle is set to 45° remains at the left tip of the lower flaw even with increasing inclination angles of the upper flaw. As the inclination angle of the lower flaw increases (see each column downwards), the fragmentation area becomes smaller, which is due to the shift of the initiation position of the ITWC originating from the lower flaw. For another ITWC emanating from the lower surface of the upper flaw, its initiation position is shifted from the middle of the lower surface of the upper flaw in the first column in Fig. 9 to at the left tip of the upper flaw (from the third column to the fifth column in Fig. 9), which is due to the increasing inclination angle of the upper flaw from β=0° to β=60°. When the inclination angle is steeper, the initiation position tends to be located at the flaw tip. This shifting behavior is also observed in the second row and the third row, irrespective of the different inclination angles of the lower flaw (α=30° and α=45°). As for the ETWC originating from the lower flaw, it initiates near the right tip of the lower flaw when the flaw is rotated 15° clockwise, while the inclination angle increases, the ETWC initiates at the right tip of the lower flaw, which is little affected by the interaction effect of the two flaws, as in the case of a single flaw (Bobet 2000, Wong 2008 and Ha *et al.* 2015). Each of the ETWC propagates downwards and then reaches the bottom of the specimen. In addition, another ETWC initiates from the right tip of the upper flaw, which is captured in all specimens from Fig. 9(a)-9(o); this means that little interacting effect between two non-parallel flaws exerts outside the bridging region between two flaws.

As the load increases, deformation becomes evident at the outer tip of the flaws, such as at the left tip of the upper flaw and at the right tip of the lower flaw. Each horsetail crack (HTC) initiates at the outer flaw tips and then propagates upwards from the right tip of the upper flaw or propagates downwards from the left tip of the lower flaw. Following the initiation of the HTC, anti-wing cracks (AWCs) initiate and propagate, yet in the opposite direction to the propagation of HTCs. With further loading, the deformation in fragmentation circumscribed by two coalescences remains but shear cracks grow in a fast and unstable manner, leading to specimen failure. Therefore, under the effect of two non-parallel flaws whose inclination angles are varied, the initiation position of the ITWC is also observed to be shifted. Furthermore, formed through the linkage of two coalescences that are induced by ITWCs, fragmentation remains constant even with further loading until other shear cracks promote specimen failure. Interestingly, the initiation position of the ETWC is at the right tip of the upper flaw or the lower flaw in all specimens, except in Figs. 9(f) and 9(k). Moreover, the ETWCs are little affected by the interaction between two non-parallel flaws.

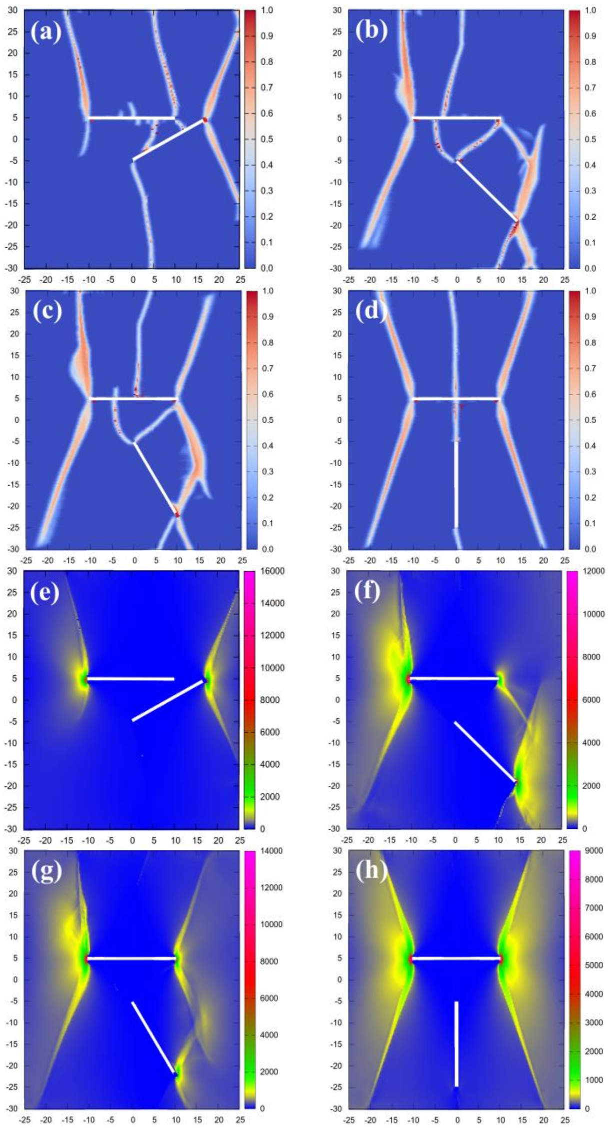

Fig. 10 Damage (the first row) and its corresponding strain energy distribution (the second row) with further loading in the flaw geometry in which both the initiation angle of the upper flaw is set to β=0° and the overlapping ratio is also set to 0.50 with varying inclination angles of the lower flaw. (a) and (e) is captured at 72 MPa for -α=30°, (b) and (f) is at 83.2 MPa for α=45°, (c) and (g) is at 88 MPa for α=60° and (d) and (h) is at 86.4 MPa for α=90

4. X-shaped shear band

After crack coalescence and fragmentation are formed by the occurrence of tensile wing cracks and shear cracks, a damage pattern, an x-shaped shear band (Huang *et al.* 1990, Chen *et al.* 1995), is observed with further loading, regardless of the effects of inclination angles and overlapping ratios mentioned in sections 2 and 3. As shown in Fig.10, the first row shows the damage caused by both tensile wing cracks (TWCs) and other shear cracks including HTCs and AWCs, while the second row shows the strain energy distribution along the newly growing cracks. As discussed in Section 3 earlier, by changing the inclination angles of the lower flaw with the horizontal upper flaw, various coalescences are formed, and corresponding shear fractures following coalescence are

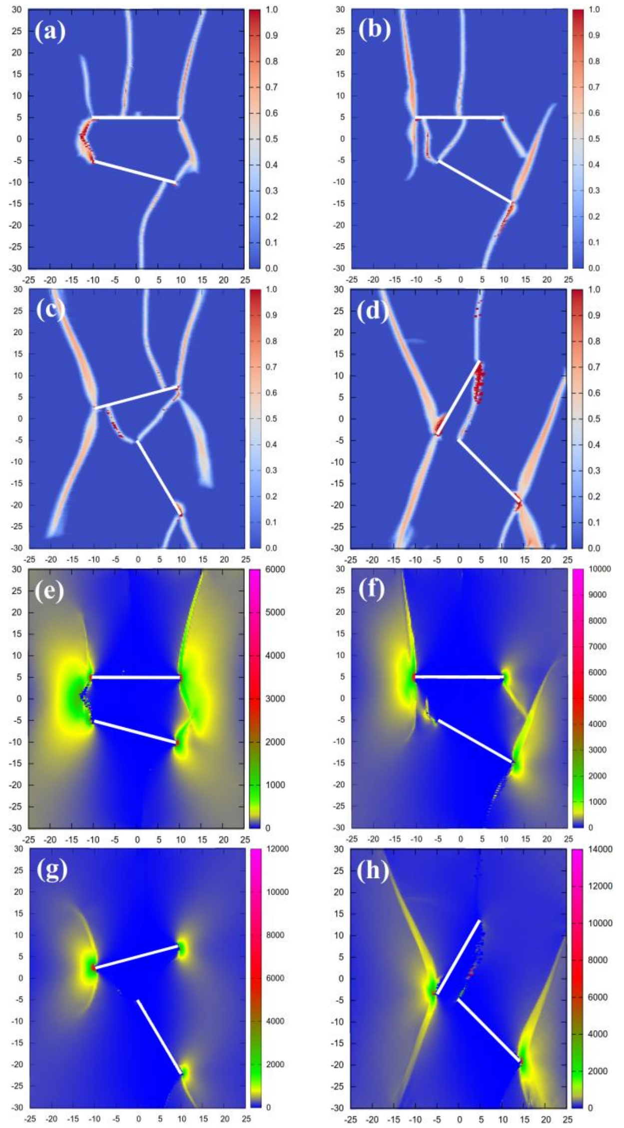

Fig. 11 Damage (the first row) and its corresponding strain energy distribution (the second row) with further loading in various flaw geometries. (a) and (e) are captured at 80 MPa for the flaw geometry where the overlapping ratio is 1.00 and the inclination angle of the lower flaw is α=15°, (b) and (f) are captured at 80 MPa for the overlapping ratio of 0.75 and the inclination of the lower flaw of α=30°, (c) and (g) are captured at 88 MPa for the overlapping ratio of 0.50, the inclination angle of the upper flaw of β=15° and the inclination angle of the lower flaw of α=60°, (d) and (h) are captured at 104 MPa for the overlapping ratio of 0.50, the inclination angle of the upper flaw of β=60° and the inclination angle of the lower flaw of α=45°

shown. In Fig. 10(a), fragmentation, created by two coalescences formed by two internal tensile wing cracks, is formed, and thereafter the TWCs and the fragmentation are retarded by growing shear cracks. With further loading, further damage in the bridging region between two non-parallel flaws does not take place, while damage outside the bridging region becomes more severe, which is due to the growth of shear cracks. Fig. 10(e) shows that crack damage ceases to progress between two flaws, but at the outmost flaw tips (left tip of the upper flaw and right tip of the lower flaw) fracturing happens in a fast and unstable manner, showing an x-shaped shear band (yellow colored). For the second column, the first fragmentation is made through two internal tensile wing cracks and the secondary fragmentation is created by an AWC initiating at the right tip of the lower flaw, or at the outmost flaw tip.

Unlike the fragmentation due to the linkage of TWCs, the fragmentation by shear cracks such as AWCs is more severe as the load increases. At the outmost flaw tip, or at the left tip of the upper flaw, a HTC emanating from the upper flaw surface and an AWC (TsS mode) (Yin *et al.* 2014) emanating from the lower flaw surface respectively reach the top and bottom of the specimen. In Fig. 10(f), it is observed that the energy concentrates obviously at two outmost flaw tips and at the second fragmentation. Similarly, in the third column in Fig. 10, two types of fragmentations are observed, and energy also concentrates at the outmost flaw tips and at the fragmentation caused by an AWC (Ts mode) (Yin *et al.* 2014), initiating at some distance from the right tip of the upper flaw. From the outmost flaw tip, an AWC initiates and coalesces with the opposite flaw, leading to a fragmentation, at the right tip of the lower flaw in the second column and at the right tip of the upper flaw in the third column. However, in the case where the lower flaw is vertically aligned, TWCs initiate at the middle of the upper flaw and reach the top and bottom of the specimen. Subsequently, at the left and right tip of the horizontal upper flaw, shear cracks initiate and then form an x-shaped shear band, which is evident in Fig. 10(h).

The first and second columns in Fig. 11 describe fragmentation modes and shear cracking patterns under the influence of the overlapping ratio. In the case of a fully overlapped flaw geometry, one fragmentation is formed both by an ITWC initiating from the left tip of the lower flaw and by an anti-wing crack from right tip of the upper flaw, since the outmost flaw tips correspond to two tips of each flaw. In fact, the ITWC propagates towards the left tip of the upper flaw and then coalesces with a HTC initiating from the right tip of the upper flaw. Each ETWC inside two flaws propagates under no interaction effect and then reaches the edge of the specimen. With further loading the shear cracks initiating from outmost flaw tips grow, leading to an x-shaped shear band, as captured in Fig. 13(e). For the overlapping ratio of 0.75, or the second column in Fig. 11, the ITWC initiates near the left tip of the upper flaw, and it reaches the left tip of the lower flaw. Another ITWC initiates at the left tip of the lower flaw and approaches the middle of the upper flaw, forming the first fragmentation. With further loading, an AWC (Ts mode) initiates at a distance from the left tip of the lower flaw and coalesces with a shear crack initiating from the right tip of the upper flaw, thereby creating the second fragmentation. Energy concentration is distinct at three points where shear cracks flourish, later forming a general x-shaped shear band. When two non-parallel flaws are rotated individually, more complicated fracturing patterns are observed as seen in the third and the fourth columns in Fig. 11. However, one fragmentation is formed through the ITWCs in the bridging region between two flaws, and outside the bridging region shear cracks propagate upwards or downwards, forming an x-shaped shear band. Through numerous simulations, general features in cracking patterns are well observed even in complex flaw arrangements. Typically, fragmentation can be created by ITWCs, and subsequent fragmentation, or secondary fragmentation, can be made by shear cracks. In addition, damage outside the bridging region between two flaws becomes more severe with further loading, thereby forming an x-shaped shear band.

5. Conclusions

In this paper, deformation and progressive failures, such as crack initiation, coalescence, fragmentation, and x-shaped shear band, are observed along with the occurrence of tensile wing cracks and shear cracks, or horsetail cracks and anti-wing cracks with varying inclination angles and overlapping ratios between a flaw pair. Showing good fidelity to physical test results, the parallelized peridynamics coupled with a finite element method presents insightful information about the cracking behavior and the cracking mechanism in complex flaw geometry such as non-parallel flaws. From the numerical results, the following conclusions can be drawn.

(1) The initiation position at which an internal tensile wing crack occurs can be shifted under the effect of the overlapping ratio as well as under the effect of the inclination angle of flaws. This shift of the initiation position plays a critical role in the first coalescence formation.

(2) Each internal tensile wing crack creates coalescence by reaching its opposite flaw; the coalescence then leads to the first fragmentation. The fragmentation is, in most cases, located inside the bridging region between two flaws and undergoes no further deformation even with further loading.

(3) Secondary fragmentation occurs through the growth of shear cracks, most of which are anti-wing cracks initiating from the outmost flaw tip. Unlike the first fragmentation, the damage from the secondary fragmentation is increased with further loading because it is substantially affected by shear cracks.

(4) As the load increases, the extent of damage inside the bridging region between two non-parallel flaws is minimal while that of damage outside the region becomes very severe.

(5) During processes such as the coalescence, the first fragmentation, and the secondary fragmentation, shear cracks initiate at the outmost flaw tips and then propagate upwards and downwards. This causes the formation of an x-shaped shear band, thereby leading to specimen failure.

Acknowledgements

This work was supported by the National Research Foundation of Korea (NRF) grant funded by the Korea government (MSIT) (No.2018R1A2A1A05019453), and was also supported by the National Research Foundation of Korea (NRF) grant funded by the Korean Government (Ministry of Science and ICT) (No. 2017R1A5A1014883).

References

Bobet, A. (2000), "The initiation of secondary cracks in compression", *Eng. Fract. Mech.*, **66**(2), 187-219.

Bobet, A. and Einstein, H.H. (1998), "Fracture coalescence in rock-type materials under uniaxial and biaxial compression", *J. Rock Mech. Min. Sci.*, **35**(7), 863-888.

Cao, P., Liu, T., Pu, C. and Lin, H. (2015), "Crack propagation and coalescence of brittle rock-like specimens with pre-existing cracks in compression", *Eng. Geol.*, **187**, 113-121.

Chen, G., Kemeny J.M. and Harpalani, S. (1995), "Fracture propagation and coalescence in marble plates with pre-cut notches under compression", *Proceedings of the Symposium on Fractured and Jointed Rock Mass*, Lake Tahoe, California, U.S.A.

Cheng, Y., Wong, L.N.Y. and Zou, C. (2015), "Experimental study on the formation of faults from en-echelon fractures in Carrara marble", *Eng. Geol.*, **195**, 312-326.

Ercolessi, F. (1997), *A Molecular Dynamics Primer*, in *Spring College in Computational Physics, ICTP*, Trieste, Italy, 24-25.

Feng, X.T., Ding, W. and Zhang, D. (2009), "Multi-crack interaction in limestone subject to stress and flaw of chemical solutions", *J. Rock Mech. Min. Sci.*, **46**(1), 159-171.

Ha, Y.D. and Bobaru, F. (2011), "Characteristics of dynamic brittle fracture captured with peridynamics", *Eng. Fract. Mech.*, **78**(6), 1156-1168.

Ha, Y.D., Lee, J. and Hong, J.W. (2015), "Fracturing patterns of rock-like materials in compression captured with peridynamics", *Eng. Fract. Mech.*, **144**, 176-193.

Haeri, H., Sarfarazi, V. and Zhu, Z. (2017), "Effect of normal load on the crack propagation from pre-existing joints using Particle Flow Code (PFC)", *Geomech. Eng.*, **19**(1), 99-110.

Huang, J.F., Chen, G.L., Zhao, Y.H. and Wang, R. (1990), "An experimental study of the strain field development prior to failure of a marble plate under compression", *Tectonophys.*, **175**(1-3), 283-290.

Ko, T.Y., Einstein, H.H. and Kemeny, J. (2006), "Crack coalescence in brittle material under cyclic loading", *Proceedings of the Golden Rocks 2006, The 41st US Symposium on Rock Mechanics (USRMS)*, Golden, Colorado, U.S.A., June.

Lajtai, E.Z. (1974), "Brittle fracture in compression", *J. Fract.*, **10**(4), 525-536.

Lee, H. and Jeon, S. (2011), "An experimental and numerical study of fracture coalescence in pre-cracked specimens under uniaxial compression", *J. Solid. Struct.*, **48**(6), 979-999.

Lee, J. and Hong, J.W. (2016b), "Dynamic crack branching and curving in brittle polymers", *J. Solid. Struct.*, **100**, 332-340.

Lee, J., Ha, Y.D. and Hong, J.W. (2017b), "Crack coalescence morphology in rock-like material under compression", *J. Fract.*, **203**(1-2), 211-236.

Lee, J., Hong, J.W. and Jung, J.W. (2017c), "The mechanism of fracture coalescence in pre-cracked rock-type material with three flaws", *Eng. Geol.*, **223**, 31-47.

Lee, J., Liu, W. and Hong, J.W. (2016a), "Impact fracture enhanced by contact of peridynamic and finite element formulations", *J. Impact Eng.*, **87**, 108-119.

Lee, J., Oh, S.E. and Hong, J.W. (2017a), "Parallel programming of a peridynamics code coupled with finite element method", *J. Fract.*, **203**(1-2), 99-114.

Li, H. and Wong, L.N.Y. (2012), "Influence of flaw inclination angle and loading condition on crack initiation and propagation", *J. Solid. Struct.*, **49**(18), 2482-2499.

Li, H.Q. and Wong, L.N.Y. (2014), "Numerical study on coalescence of pre-existing flaw pairs in rock-like material", *Rock Mech. Rock Eng.*, **47**(6), 2087-2105.

Liu, W. and Hong, J.W. (2012a), "Discretized peridynamics for linear elastic solids", *Comput. Mech.*, **50**(5), 579-590.

Liu, W. and Hong, J.W. (2012b), "Discretized peridynamics for brittle and ductile solids", *J. Numer. Mech. Eng.*, **89**(8), 1028-1046.

Liu, W. and Hong, J.W. (2012c), "A coupling approach of discretized peridynamics with finite element method", *Comput. Meth. Appl. Mech.*, **245**, 163-175.

Manouchehrian, A. and Marji, M.F. (2012), "Numerical analysis of confinement effect on crack propagation mechanism from a flaw in a pre-cracked rock under compression", *Acta Mech. Sinica*, **28**(5), 1389-1397.

Manouchehrian, A., Sharifzadeh, M., Marji, M.F. and Gholamnejad, J. (2014), "A bonded particle model for analysis of the flaw orientation effect on crack propagation mechanism in brittle materials under compression", *Arch. Civ. Mech. Eng.*, **14**(1), 40-52.

Mughieda, O. and Alzo'ubi, A.K. (2004), "Fracture mechanics of offset rock joints: a laboratory investigation", *Geotech. Geol. Eng.*, **22**(4), 545-562.

Park, C.H. and Bobet, A. (2009), "Crack coalescence in specimens with open and closed flaws: A comparison", *J. Rock Mech. Min. Sci.*, **46**(5), 819-829.

Park, C.H. and Bobet, A. (2010), "Crack initiation, propagation and coalescence from frictional flaws in uniaxial compression", *Eng. Fract. Mech.*, **77**(14), 2727-2748.

Sagong, M. and Bobet, A. (2002), "Coalescence of multiple flaws in a rock-model material in uniaxial compression", *J. Rock Mech. Min. Sci.*, **39**(2), 229-241.

Sarfarazi, V. and Haeri, H. (2016), "A review of experimental and numerical investigations about crack propagation", *Geomech. Eng.*, **18**(2), 235-266.

Shen, B., Stephansson, O., Einstein, H.H. and Ghahreman, B. (1995), "Coalescence of fractures under shear stress experiments", *J. Geophys. Res.*, **100**(6), 5975-5990.

Silling, S.A. (2000), "Reformulation of elasticity theory for discontinuities and long-range forces", *J. Mech. Phys. Solids*, **48**(1), 175-209.

Silling, S.A. and Askari, E. (2005), "A meshfree method based on the peridynamic model of solid mechanics", *Comput. Struct.*, **83**(17-18), 1526-1535.

Tang, C.A. and Kou, S.Q. (1998), "Crack propagation and coalescence in brittle materials under compression", *Eng. Fract. Mech.*, **61**(3-4), 311-324.

Tang, C.A., Lin, P., Wong, R.H.C. and Chau, K.T. (2001), "Analysis of crack coalescence in rock-like materials containing three flaws-Part II: Numerical approach", *J. Rock Mech. Min. Sci.*, **38**(7), 925-939.

Tian, W.L. and Yang, S.Q. (2017), "Experimental and numerical study on the fracture coalescence behavior of rock-like materials containing two non-coplanar filld fissures under uniaxial compression", *Geomech. Eng.*, **12**(3), 541-560.

Wong, L.N.Y. (2008), "Crack coalescence in molded gypsum and Carrara marble", Ph.D. Dissertation, Massachusetts Institute of Technology, Cambridge, Massachusetts, U.S.A.

Wong, L.N.Y. and Einstein, H.H. (2009a), "Systematic evaluation of cracking behavior in specimens containing single flaws under uniaxial compression", *J. Rock Mech. Min. Sci.*, **46**(2), 239-249.

Wong, L.N.Y. and Einstein, H.H. (2009b), "Crack coalescence in molded gypsum and Carrara marble: Part 1. Macroscopic observations and interpretation", *Rock Mech. Rock Eng.*, **42**(3), 475-511.

Wong, R.H.C., Chau, K.T., Tang, C.A. and Lin, P. (2001), "Analysis of crack coalescence in rock-like materials containing three flaws-Part I: Experimental approach", *J. Rock Mech. Min. Sci.*, **38**(7), 909-924.

Wong, R.H.C., Guo, Y.S.H., Li, L.Y., Chau, K.T., Zhu, W.S. and Li, S.C. (2006), "Anti-wing crack growth from surface flaw in real rock under uniaxial compression", *Proceedings of the 16th European Conference of Fracture (EFC16)*, Alexandroupolis, Greece, July.

Wong, R.H.C., Tang, C.A., Chau, K.T. and Lin, P. (2002), "Splitting failure in brittle rocks containing pre-existing flaws under uniaxial compression", *Eng. Fract. Mech.*, **69**(17), 1853-1871.

Wu, Z. and Wong, L.N.Y. (2014), "Investigating the effects of micro-defects on the dynamic properties of rock using numerical manifold method", *Constr. Build. Mater.*, **72**, 72-82.

Yang, S.Q., Yang, D.S., Jing, H.W., Li, Y.H. and Wang, S.Y. (2012), "An experimental study of the fracture coalescence behaviour of brittle sandstone specimens containing three fissures", *Rock Mech. Rock Eng.*, **45**(4), 563-582.

Yin, P., Wong R.H.C. and Chau, K.T. (2014), "Coalescence of two parallel pre-existing surface cracks in granite", *J. Rock Mech. Min. Sci.*, **68**, 66-88.

Zhang, X.P. and Wong, L.N.Y. (2013), "Crack initiation, propagation and coalescence in rock-like material containing two flaws: A numerical study based on bonded-particle model approach", *Rock Mech. Rock Eng.*, **46**(5), 1001-1021.

Zhou, X.P., Bi, J. and Qian, H. (2015), "Numerical simulation of crack growth and coalescence in rock-like materials containing multiple pre-existing flaws", *Rock Mech. Rock Eng.*, **48**(3), 1097-1114.

Zhou, X.P., Cheng, H. and Feng, Y.F. (2014), "An experimental study of crack coalescence behaviour in rock-like materials containing multiple flaws under uniaxial compression", *Rock Mech. Rock Eng.*, **47**(6), 1961-1986.

GC